Annalen der Physik / Volume 535, Issue 10 / 2300218

Research Article | Full Access

Infrared Absorber Leveling in Ultra-Wideband by Using Hybrid Plasmonic Structure

Xing Yu Xu, Zhong Zhu Liang, Li Qin, Xue Mei Su

First published: 15 September 2023
https://doi-org.fgul.idm.oclc.org/10.1002/andp.202300218

Abstract

In this paper, an effective ultra-broadband absorber in long-wavelength infrared is achieved by a metal-insulator-metasurface (MIM) stacked structure. This absorber exhibits an average absorption of 90% at wavelengths ranging from 8 to 14 μm and a maximum absorption rate of up to 97.1%. It is found that the performance is achieved by three mode combinations. The ultra-broadband leveling absorber is to be polarization-independent due to its geometrical symmetry. The absorption property can be controlled by the parameters of the triangle unit. It has great potential in many applications such as infrared detection and imaging.

1 Introduction

Since the first proposal is used to achieve perfect absorption by plasmonic structure in 2008,[1] more and more attention is drawn to the absorbers because they can apply in fields of solar cells, sensors, bolometers, and imaging equipment.[2-4] With developments of meta-surface materials,[5] various manners are used for controllation and tunable light absorptions in dual-band, multi-band, wideband, and narrow-band. People are devoted to the applications in accurate operations in quick-response sensors[6-9] in single narrow absorption bands, precise infrared detectors, and high absorptivity solar cells in the atmosphere[10-19] in the ultrabroad band. Many technologies have been developed to construct absorbers with high absorptivity in an ultra-wideband (UWB). For example, an infrared absorber made of saw-toothed anisotropic metamaterial could achieve more than 90% absorptivity in the continuous spectrum range of 3000 to 5000 nm.[21] An UWB polarization-independent metamaterial is absorbed by using different side lengths to reach

different absorption modes,[22] which is composed of a periodic array of multilayered quadrangular frustum pyramids. Some graphene-based absorbers have been proposed to control its absorption.[23, 24] Most of these applications greatly benefit from novel functions and extraordinary properties of metamaterial structures. By manipulating magnetic and electrical resonance, high absorption of the incident light can be achieved. The absorber structure can be designed based on analyses from reflectance and transmittance of input light by solutions to Maxwell equations of the structures.

In this paper, we proposed a scheme by using a triangular metal prism to construct a periodic arrangement of resonant units and realize an ultra-broadband tunable infrared absorber. The multipolar modes of the hybrid structure combination are analyzed. Each square resonant unit has four triangle prisms on the top surface with metal Ti, which has a higher melting point and larger absorption rate than noble metals in refractory Plasmonics.[25] The asymmetry of triangles in the symmetry of the resonant unit takes effect on the multi-polar resonant modes and therefore leads to superior performance and application prospects. The structure is insensitive to the polarization direction of the incident light. The excited modes include the propagating surface plasmon resonance (PSPR), local surface plasmon resonance (LSPR), and the resonance of Fabry–Perot (FP) cavity. It is shown that the less-layer metamaterials are one of the most important structures as broadband, efficient, ultra-thin metal-insulator-metal (MIM) absorbers by utilizing metals with high imaginary part of permittivity.[26] Here, the complex MIM structure exhibits better symmetric and asymmetric properties in absorptivity spectra for a nearly perfect absorber. The leveling high absorption in the ultrabroad infrared range benefits from the effects of coherence and interference between the excitation modes.

Many methods[27] are applied in excitation mode combinations, such as using an ultra-thin random metasurface to couple two modes of different shapes of units.[28] By using disorder to induce interaction between guided modes and a flat band of low-Q radiating modes in planar arrays of dielectric particles, it can be realized frequency selective omnidirectional scattering of light.[29] An ultra-thin refractory titanium, a refractory[25] titanium nitride meta-surface with efficient, ultra-broadband solar energy absorption has been designed and numerically demonstrated. In Ref.[[30]], a 250 nm thick ultra-thin meta-surface absorber, taking the absorptivity A > 90% into account, an 1110 nm spectral bandwidth over the whole ultraviolet-visible-near infrared (UV–vis–NIR) range is achieved. Here, a common photon in a waveguide cavity is utilized to combine three hybrid modes with a 30 nm thick meta-surface MIM absorber, leading to the same order of absorptivity and leveling spectral bandwidth in the mid- and far-infrared range. We analyzed the influence of different materials and structural parameters on the absorption of the absorber. It was proven that the proposed absorber had the characteristics of wider polarization angle insensitivity to the input light or polarization independence. At present, the preparation and measurement technologies of absorbers with different micro/nano-structures or metamaterials are becoming more and more mature. The proposed four-layer absorber can be fabricated easily because the width

of the prism is in order of μm, thickness in order 500 nm. It can be generated by using the radio-frequency sputtering or E-beam to deposit the four-layer thin films or using the lithography process and different etching processes to construct the triangular prisms in Ge and Ti films.[3]A great application prospect is worth expecting for its ultra-wideband, easy manufacturing, angle insensitive, or polarization independence.

2 Geometric Dimensions of the Devices

The schematic of the designed absorber was structured, as shown in **Figure 1a** where an upper layer of triangular Ti cubes and a bottom layer of Ti film were separated by a layer of Ge dielectrics. This was a new metamaterial-insulator-metal (MIM) structure[26] with an array of right-angled triangular resonant units on the left of the yellow arrow, as shown in Figure 1a. On the right was the enlarged diagram of the unit cell of the absorber. Each unit cell included four triangles that were located in the middle of the four sides of rectangles and the apexes of every two angles were opposite. Due to the symmetry of the unit cells, absorption of the designed plasmonic resonator was polarization direction insensitive. The third subgraph in Figure 1a was a lateral diagram of the absorber. The underlying metal *Ti* layer was thick enough to prevent light transmission and the surrounding material was set to air. The dielectric layer material was Ge and was relatively transparent in the infrared region. It could significantly reduce the thickness of the structure compared to other dielectric materials in the infrared regime. Here, the metal resonator unit was an isosceles right-angled triangular. Its hypotenuse length d was in the same order of μm as the wavelength of input light and its thickness t_1 was less than the skin depth of metal Ti for mixed excitation between different modes, and here the optimum t_1 was ≈30 nm. The depths of Ge dielectrics and the uniform metal film in the bottom were t_2 and t_3, respectively.

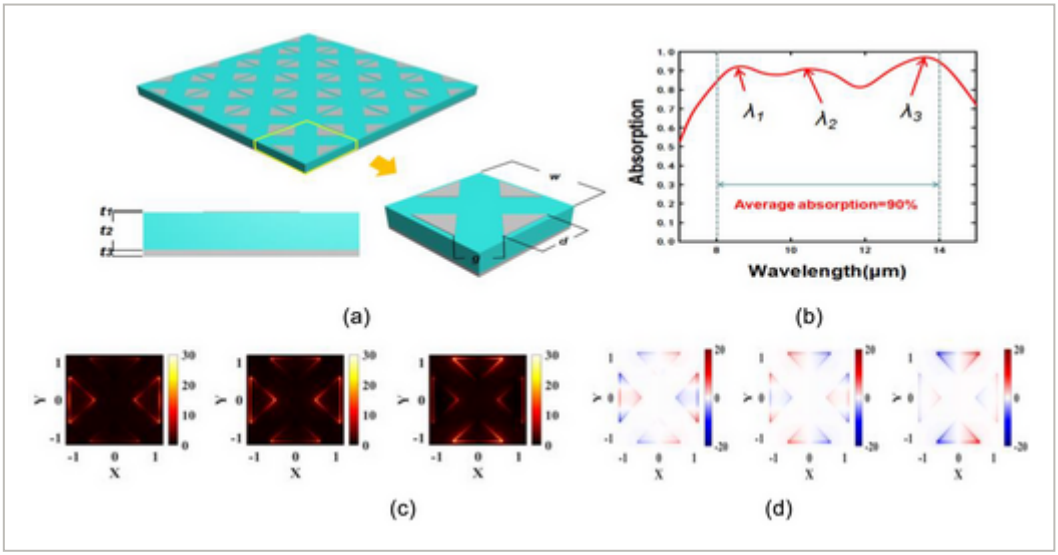

Figure 1

Open in figure viewer | PowerPoint

Schematic diagrams of the proposed broadband meta-material absorber (upper), the magnified unit cell (yellow arrow pointed), and lateral diagram including thicknesses of metallic cubes t_1, middle Ge layer t_2, and below Ti film t_3. b) The absorption spectrum of the proposed absorber by parameters of the unit cell are as w = 2.4 μm, d = 1.2 μμm, t_1 = 30 nm, t_2 = 530 nm, t_3 = 100 nm, and space of every adjacent unit is 200 nm. c,d) Electric field and surface charge distributions at resonance wavelengths 8.9, 10.8, and 13.5 μm (colored bar in x–z plane, y = 0).

The absorption spectrum of the absorber is depicted in Figure 1b by incident light normally entering the surface. It showed high absorptivity (>90%) in the wavelength range between 8 and 14 μm and bandwidth (BW) up to 1100 nm. The absorptions of the three resonance peaks marked λ_1, λ_2, and λ_3 reached 91%, 90%, and 97.1%, respectively, as shown in Figure 1b. The input light caused polarization of each MIM cell and thus led to distributions of the surface plasmon field and surface polarized charge, in Figure 1c,d correspondingly.

3 Results and Discussion

3.1 Analyses of Resonant Modes

Compared with previous reports, this device is creative in feathers with thinner cubes whose thicknesses are smaller than the skin depth of the metal. As mentioned in Ref.[[1]], the thick cubes have the corresponding resonant wavelengths λ_1, λ_2, and λ_3 are dependent twice of the effective lengths√2d, 2d, 2√2d, multiplied by refractive index at interface[1] $(\varepsilon n_2^2/(\varepsilon+n_2^2))^{1/2}$; d is the hypotenuse length of the metallic cubes. When the thickness of the metallic cubes is less than the skin depth (t_{skin}) of metal Ti, electrons can pass through the metallic cubes and populate on the top and bottom surfaces. The fourth resonant mode of SPP oscillation is created in the lateral plane with effective lengths $\Lambda_4 = w*n_{in2}$ (w, width of a unit cell, $n_{in2} = (\varepsilon n_0^2/(\varepsilon + n_0^2))^{1/2}$. It is hybridized with the three resonant modes to generate three hybrid modes with effective lengths $\Lambda_{1h,2h,3h} = \sqrt{\Lambda_{1,2,3}^2 + \Lambda_4^2}$. The three hybrid modes can be coupled by a common cavity photon in the waveguide cavity. This leads to high absorption and absorption leveling. The waveguide cavity[30] is formed by a series of 2D microcavities, each of which includes metallic cubes on the top surface, a middle of dielectric, and a uniform metal layer on the bottom to couple with individual SPP waves at the interface and leads to high absorption at each mode of SPP waves as electromagnetically induced absorption. In the following section, we quantitatively analyze the strong coupling of intracavity photons with hybrid SPP waves and explain the essence of absorption leveling in an ultrawide range.

3.2 Hybrid Modes in a Dipole–Waveguide Cavity with Thinner Cubes

We begin by building interaction equations for the hybrid modes whose average field amplitudes are expressed by $b_j(\omega)$ (j = 1, 2, 3) and the cavity photons in a four-level system, as shown in **Figure 2a**. It describes couplings between SPP dipoles with a common photon in

a waveguide cavity. The photons are described by the creative operator $a^{\dagger}$ (annihilation operator a), where $a(\omega)$ is the average field amplitude in a microcavity.[31]

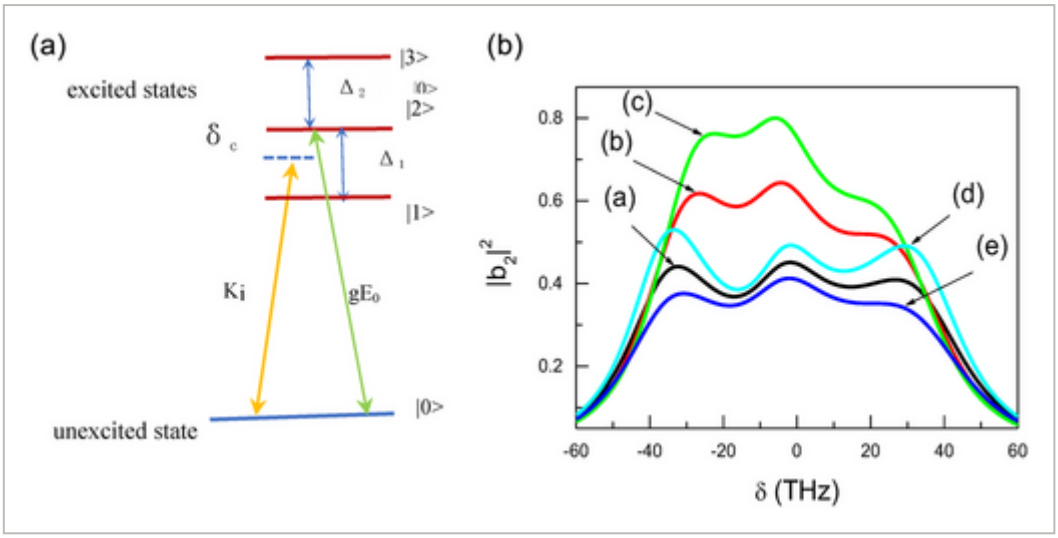

Figure 2

Open in figure viewer | PowerPoint

a) Simplified energy level diagram for the system. b) absorption spectra versus frequency detuning δ to show plasma absorption leveling from solution to Equation (1).

The field amplitudes are dependent on the Langevine equations in the frequency space[32] as

$$\begin{matrix} a \\ b_1 \\ b_2 \\ b_3 \end{matrix} = -M \begin{matrix} 0 \\ 0 \\ gE_0 \\ 0 \end{matrix} \tag{1}$$

$$M = \begin{matrix} \delta + \Delta_c + i\gamma_c & \kappa_1 & \kappa_2 & \kappa_3 \\ \kappa_1 & (\delta - \Delta_1) + i\gamma_1 & \chi_{12} & \chi_{13} \\ \kappa_2 & \chi_{21} & \delta + \delta_0 + i\gamma_2 & \chi_{23} \\ \kappa_3 & \chi_{31} & \chi_{32} & (\delta + \Delta_2) + i\gamma_3 \end{matrix}^{-1} \tag{2}$$

where the coupling strengths χ_{ij} between hybrid modes in nonlinear processes and their coupling with cavity photons by strengths κ_i (i = 1, 2, 3) under condition $\kappa_i >> \chi_{ij}$ (i, j = 1, 2, 3); $\Delta_1 = (\omega_1 - \omega_0)$, $\Delta_2 = (\omega_3 - \omega_0)$, $\delta_0 = (\omega_2 - \omega_0)$, $\Delta_c = (\omega_c - \omega_0)$ are frequency detunings from the center frequency $\omega_0 = (\omega_1 + \omega_3) / 2$ and variable $\delta = (\omega - - \omega_0)$. The frequencies of the hybrid modes 1 and 3 detuned from that of the intracavity photon are as $\Delta_{c1,2} = (\Delta_{1,2} - \Delta_c)$. Rabi frequency of the incident light gE_0 represents its strength, and E_0 is the amplitude of the electric field component.

The resonant frequencies $\omega_j = 2\pi c/\lambda_j$ (j = 1, 2, 3) of the dipoles in the hybrid modes with respect to the transitions from the unexcited state $|0>$ to excited states $|j>$. The parameters $\chi_{ij} = \sqrt{\gamma_i \gamma_j}$ stands for coupling strength between two hybrid modes owing to dipole–dipole interaction.[33] It is dependent on the susceptibility of itself $\alpha_s = \frac{A}{[(\omega - \omega_{spp}) + i\gamma_{spp}]}$ by Drude model (A is SPP oscillation strength[34]) and impact from other units on meta-surface, namely lattice sum, by a term of $S = \sum S_j$;(j = 1,2,3...N-1). S_j is dependent on the distance r_j between the ith and jth units. It results in a frequency shift $\Omega_i = A\mathrm{Re}(S)$ and collective damping rate $\gamma_i = \gamma_{spp} + A\mathrm{Im}(S)$.[34]

Here, the incident light illuminates arrays of microcavities with the dispersion relation $\omega_k = (\omega_c - 2J\cos k)$ [24] in a bandwidth of 4J around the center frequency ω_c. Because the dense microcavities are periodically placed as a grating with a grating constant of a unit whose width u, the bandwidth of the guide cavity is equal to that of the corresponding grating[35] $4J \sim \omega_g = c\pi/L*\Delta n$, which is ultrawide for large refractive index differences Δn, the effective repetitive period $L = n * u + p$, and p is separation of the neighboring units. The plasma dipoles and photons in the waveguide microcavity at position r_i are coupled by strength $\kappa_{ij} = g_{0i}^2 F_{ij}$ where $g_{0i} = |\mu_i| \sqrt{\frac{\omega_c}{2\hbar\varepsilon_0 V}}$ (i = 1, 2, 3), [36]which is dependent to itself and as well as interacting with inter-microcavities by $F_{ij} = \frac{2e^{iqr_j}}{v(\Delta_{ci})}$; here the group velocity of mode 1 and 3 is $v(\Delta_c) \approx \sqrt{(2J)^2 - (\Delta_{ci})^2}$ (i = 1, 2). The phase shift in term $e^{i\xi}$ [31] is $\xi = qr_j$ and $q = k\beta_0 / 2$ [37] results from the fact that the incident field controls the intracavity EIT medium, pulling the frequencies of photons into a broad bandwidth. The wavevector of the incident light is $k = 2\pi / \lambda_0$, and the real part of the atomic susceptibility $\beta_0 = (1 - \arccos(\frac{\Delta_{ci}}{2J}) / \pi)$. The collective decay rate, $\gamma_i = g_{0i}^2 F_i$,[30] can be calculated by the coupling strength of a single microcavity, g_{0i}, and the parameters of inter-microcavities $F_i = \sum_j |\frac{2\cos\xi}{v(\Delta_c)}|$. The collective spontaneous emission coherence constant is[30] $\kappa_i = \frac{3\gamma_i}{2} \sum_{j=1}^{\pi / k_0 w} S_j$; $S_j = -\frac{\cos\xi}{\xi} + \frac{\sin\xi}{\xi^2} + \frac{\cos\xi}{\xi^3}$ under the condition that the angle $\alpha = \pi/2$ between the dipole moment μ_i and vector r_j. The parameters of dispersion parameters, β_0, group velocity, v, and inter-microcavities, F, are obtained as shown in **Table 1** for a symmetric cavity under $\Delta_c = 0$. The absorption of the intracavity medium is $\chi = \frac{gN^2(\kappa_3^2(\delta - \Delta_1 + i\gamma_1) + \kappa_1^2(\delta + \Delta_2 + i\gamma_3) - C(\delta + \Delta_2 + i\gamma_3))}{B(\delta - \Delta_1 + i\gamma_1) - (C - \kappa_1^2)(\delta + \delta_0 + i\gamma_2)(\delta + \Delta_2 + i\gamma_3)}$;
$B = -\kappa_3^2(\delta + \delta_0 + i\gamma_2) - \kappa_2^2(\delta + \Delta_2 + i\gamma_3)$ and $C = (\delta - \Delta_1 + i\gamma_1)(\delta + \Delta_c + i\gamma_c)$.

Table 1. Symmetric cavity parameters for Figure 3b.

Mode	β_0	F	g_i [THz]	γ_i [THz]	$1.5\gamma_i\cos\xi / \xi^3$
1	0.78	0.053	19.0	19.0	$7.1\gamma_1$
2	0.52	0.041	17.5	12.6	$20.0\gamma_1$

Mode	β_0	F	g_i [THz]	γ_i [THz]	$1.5\gamma_i\cos\xi / \xi^3$
3	0.78	0.053	17.5	16.2	$6.0\gamma_1$

From Table 1, the collective Rabi frequency of mode 2 is larger than the sum of half of the widths of the three modes under $\Delta_c = 0$, and thus the three modes of SPP waves can be combined by a common intracavity photon as shown in curve (a) of Figure 2b. However, coupling with photons in an asymmetrical cavity under $\Delta_c \neq 0$ in curves (b)-(e), only one more mode combines with the middle mode as in curves (b)-(e). This results in absorption leveling in a comparatively narrower bandwidth compared with a situation under three mode combination. The absorption spectra in Figure 2b show the effect of the mode combination in the waveguide cavity that leads to absorption leveling.

The system can reach $\Delta_c \neq 0$ by varying the parameters of the metasurface and microcavity, such as by different inter-unit space and the insulator thickness. To analyze the effect of metallic gratings on absorption leveling, we compare the bandwidth of the intracavity photon in absorption with metallic gratings in symmetric (curve (a)) and asymmetric (curves (b) and (d)) waveguide cavities whose parameters are shown in **Table 2**. The bandwidths of the gratings are estimated as $2J$ = 46.5 THz.[30] The left and right edges located at $\Delta_l = -2J + \Delta_c$ and $\Delta_r = 2J + \Delta_c$[38] are symmetric with respect to the frequency of a single microcavity ω_c when $\Delta_c = 0$ but asymmetrically when $\Delta_c \neq 0$. The parameters used for curves (b)-(e) of Figure 2b are w = 2.4 μm, t_2 = 590 nm for curve (b); w = 2.8 μm and t_2 = 590 nm for curve (c); t_2 = 530 nm, w = 2.4 μm for curve (d) and t_2 = 629 nm and w = 2.4 μm for curve (e) by keeping the positions and orientations of the metallic cubes in each unit unchanged.

Table 2. Band edges for symmetric and asymmetric cavities Figure 2b.

Curves	Left edge	Right edge	Δ_{c1}	Δ_{c2}	Mode-combined
(a)	$-3.6\gamma_2$	$3.6\gamma_2$	$-2.8\gamma_2$	$2.8\gamma_2$	Modes 1, 2, 3
(b)	$-4.0\gamma_2$	$2.8\gamma_2$	$-1.9\gamma_2$	$3.1\gamma_2$	Mode 1 and 2
(d)	$-2.7\gamma_2$	$4.5\gamma_2$	$-3.7\gamma_2$	$1.9\gamma_2$	Mode 2 and 3

Here, the physical essence of absorption leveling is based on phase EIT, similar to gain leveling in Er^{3+}-doped fibers [39] except for population transfer without incoherent pumping. According to the parameters in Table 1, the coupling strengths are enhanced owing to the phase coherence for absorption leveling, which benefits the impact of inter-microcavities. It creates a large collective decay rate and strong Rabi frequency on the second mode, which is

directly illuminated by incident light and combined with the other two modes by common intracavity photon to realize absorption leveling in a wider bandwidth. This is based on the effect of the phase EIT in a waveguide cavity due to combinations of the three modes.

3.3 Collective Coupling and Frequency of Intracavity Photon with Hybrid Modes

Based on the above analyses, the waveguide cavity exerts influence on the hybrid modes combinations in two ways. One is from large collective coupling which is decided by the separation of each neighboring unit due to dipole–dipole interaction; the other is dependent on frequency detuning between intracavity photon and central frequency of the three modes. Since the coupling strength of the dipole–dipole effect is mainly proportional to $(w/\lambda_c)^{-3}$, the larger the distance of the adjacent unit w, the larger the absorption leveling range. We depicted absorption spectra at several unit widths w, in **Figure** 3a by using the FDTD solution software. A larger distance, such as w = 3 μm, that is small collective strength, leads to a smaller range of absorption leveling than a structure with w = 2.8 μm although the mode combination happens in the same two modes. A smaller distance of neighboring units w = 2.4 μm, leads to more modes coupling, so a much wider range of absorption leveling.

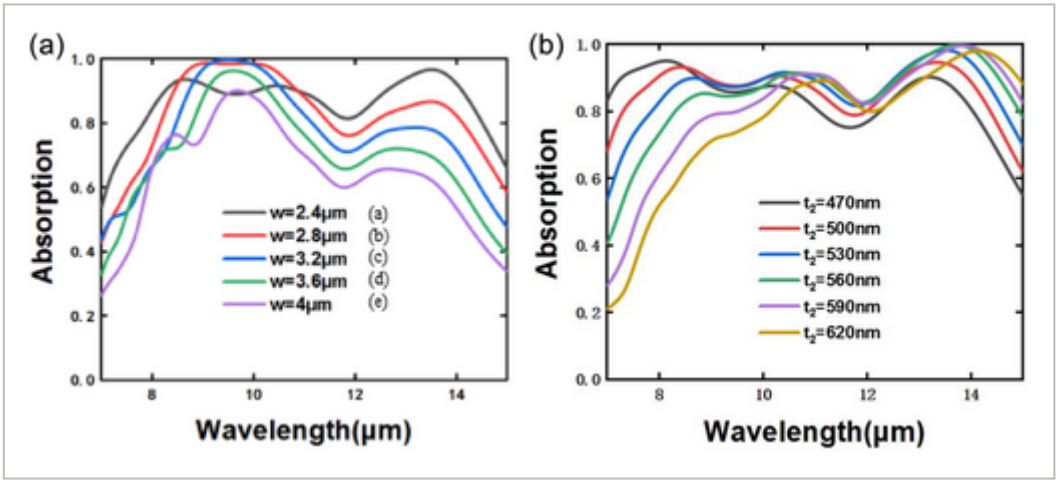

Figure 3

Open in figure viewer | PowerPoint

Absorption spectra (a) and (b) are dependent on distances "w", and thickness t_2 by FDTD solution software.

The thickness of waveguide microcavity is one of the main elements for the frequency of intracavity photon which can alter value Δ_c. The absorption spectra at different thicknesses t_2 are drawn in Figure 3b by keeping w = 2.4 μm. Figure 3b is used to indicate the advantages of the dipole–dipole effect. Absorption curves at several frequency detunings Δ_c obtained under w = 2.4 μm in Figure 3b. It demonstrates that the phase coherence of a symmetrical waveguide cavity (blue curve) can reach a wider range of absorption leveling. The positions of the central mode and ranges of absorption leveling depend on Δ_c. The other curves

correspond to different detunings Δ_c which are negative and positive, and therefore, lead to coupling of the resonant SPP wave with the first or the third modes. The optimum thickness t_2 = 530 nm happens as shown in blue curve. The corresponding absorption spectra exhibit accordant results with analyses in Figure 2b under the frequency detuning Δ_c.

3.4 Tunability of the Triangular Unit

The triangular resonant unit structure shows excellent tunability. A wider absorption is expected by adjusting the size of the plasmonic resonance structure. We depict absorption spectra at different hypotenuse lengths of each right-angled triangle in a resonant unit to determine the size of the resonant unit and keep separations fixed between two opposite triangles in each unit. By dealing with a triangular prism equivalently as a metallic stripe[41] and analyzing resonant frequencies of every unit with a varying width of metallic stripe using the equivalent LC circuit models,[41] we find that with hypotenuse length d being increased, separations of adjacent and opposite triangles being decreased in every unit, the resonant absorptions at modes 1 and 3 blue- and red-shift, respectively, with large and small scopes, as shown in **Figure** 4a. The resonant wavelength of the second mode is almost unchanged due to the fixed separation of adjacent units. These effects lead to leveling range being elongated. Although the absorption rate decreases to a certain extent with the size of triangles being enlarged, it is still high enough over 80% in an ultra-wide bandwidth.

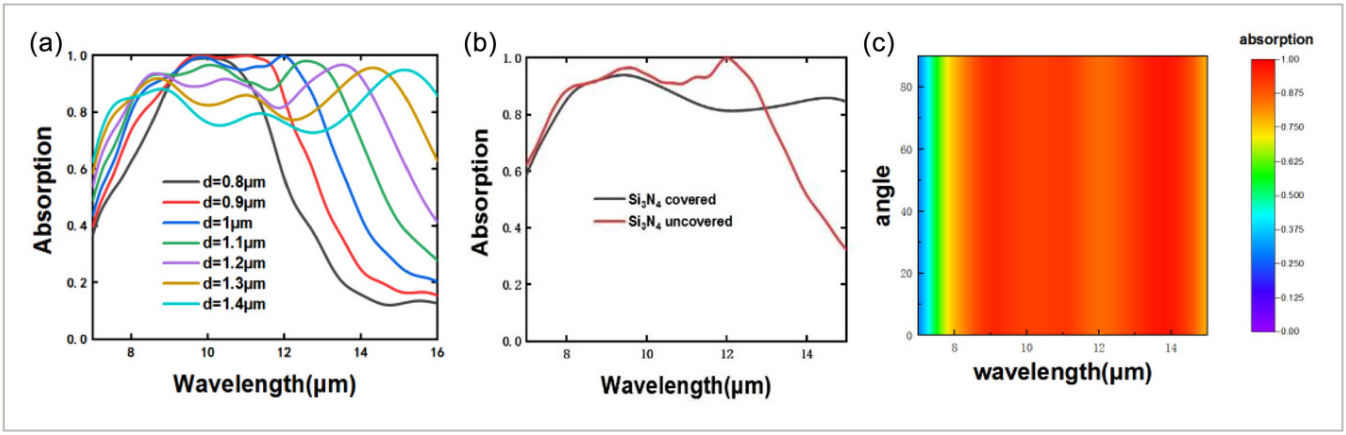

Figure 4

Open in figure viewer | PowerPoint

Absorption spectrum a) at different sizes of the metallic triangles. b) with and without Si_3N_4-covered layers. c) with different polarization angles.

Based on the above analyses, the degree of absorption leveling, defined as the difference between the highest and lowest absorption in leveling range, is found to be dependent on several associated parameters of the MIM structure. We choose optimum leveling curves in Figure 4a at hypotenuse length d = 1 and thickness of middle dielectric layer t_2 = 500 nm for a proper center frequency of waveguide cavity to find other factors to enlarge leveling range.

And then we modulate absorptions with a covering layer of Si_3N_4 (refractive index n_c = 1.4) on the surface and find in a covered cavity, the resonant wavelength λ_3 red-shift in a wide range based on modulation of absorption rate at mode 3 by intracavity EIT technique as shown in Figure **4b**. The higher leveling degree in 8–14 μm is created which is in accordance with prediction and analyses by varying refractive index.[41] On the other hand, it is useful to prevent from corrosion of metal on meta-surface in the air.

3.5 Polarization-Angle Insensitive Property

In the following, we will demonstrate it is not insensitive to polarization angle. We study the dependence of broadband absorber polarization on oblique incidence. From Figure **4c**, as the polarization angle increases from 0° to 90°, the absorbance does not substantially change whether for TE (electric field in the y-direction) mode or TM (magnetic field in the y-direction). The system is showing a high degree of polarization insensitivity. This mainly resulted from the high-degree symmetry of four triangles in the structure. The SPP waves can be illuminated by diffracted incoming light since they can be diffracted by the meta-surface along the vertical or parallel direction and then drive the SPP waves within the interface between the upper surface and middle layer. Absorption is dependent on structure but the strength of input light. When the polarization is at any angle, each resonant unit can create the same resonant excitation, thereby avoiding the decrease in the absorption rate. We can achieve an ultra-wideband absorption structure of 8–14 μm omnidirectional and polarization insensitive. This has extremely high application value in the field of atmospheric infrared detection and imaging.

4 Conclusion

In this paper, we propose a periodic triangular resonant unit structure made of MIM structure Ti/Ge/Ti. The field amplitude equations for a dipole–waveguide cavity is built to find and prove the essence of plasma absorption leveling. This is created by phase coherence from arrays of microcavities induced by the coupling of three hybrid modes under incident light illumination. The vertically propagating incoming light can be diffracted into the middle layer of the insulator Ge, benefiting traditional diffraction from the metasurface and driving SPP excitation in the three hybrid modes. In a waveguide, cavity photons couple with multiple plasmonic dipoles at resonance to enhance the coupling strength, leading to high absorption and absorption leveling. With incident light illumination, three or two hybrid modes are combined, resulting in plasma absorption leveling. Three subsystems are configured for absorption leveling similarly as those for gain leveling in Er^{3+}-doped fibers. One is nearly resonant to the driving field, and the other two have large detuning.

In addition, we find that the leveling range is independent of the polarization angle of the incident light owing to the symmetric arrangements of every unit on the meta-surface. This makes it easy to be utilized in atmospheric environments, regardless of oblique incidence.

The performance of the absorber also provides a new way of the design of the absorber and has broad application prospects in practical applications such as optical detection and imaging.

Acknowledgements

The authors acknowledge financial support by the National Natural Science Foundation of China under Grant No.11174109.

Conflict of Interest

The authors declare no conflict of interest.

Open Research

Data Availability Statement

The data that support the findings of this study are available from the corresponding author upon reasonable request.

References

1 H. Lin, B. C. Sturmberg, K.-T. Lin, Y. Yang, X. Zheng, T. K. Chong, C. M. de Sterke, B. Jia, *Nat. Photonics* 2019, **13**, 270.

CAS | Web of Science® | Google Scholar

2 T. Wanghuang, W. Chen, Y. Huang, G. Wen, *AIP Adv.* 2013, **3**, 102118.

Web of Science® | Google Scholar

3 T. D. Dao, K. Chen, S. Ishii, A. Ohi, T. Nabatame, M. Kitajima, T. Nagao, *ACS Photonics* 2013, **2**, 964.

Web of Science® | Google Scholar

4 L. Feng, P. Huo, Y. Liang, T. Xu, *Adv. Mater.* 2013, **32**, 1903787.

Google Scholar

5 S. Zong, D. Zeng, W. Yuan, G. Liu, Z. Liu, *Chin. Opt. Lett.* 2022, **20**, 073603.

Google Scholar

6 N. I. Landy, S. Sajuyigbe, J. J. Mock, D. R. Smith, W. J. Padilla, *Phys. Rev.* 2008, **100**, 207402.

CAS | Google Scholar

7 K.-T. Lee, C. Ji, L. J. Guo, *Appl. Phys. Lett.* 2016, **108**, 031107.

CAS | Web of Science® | Google Scholar

8 Z. Liu, X. Liu, S. Huang, P. Pan, J. Chen, G. Liu, G. Gu, *ACS Appl. Mater. Interfaces* 2015, **7**, 4962.

CAS | PubMed | Web of Science® | Google Scholar

9 M. Luo, S. Shen, L. Zhou, S. Wu, Y. Zhou, L. Chen, *Opt. Express* 2017, **25**, 16715.

CAS | PubMed | Web of Science® | Google Scholar

10 Y. Q. Ye, Y. Jin, S. He, *J. Opt. Soc. Am B* 2010, **27**, 498.

CAS | Web of Science® | Google Scholar

11 K. Aydin, V. E. Ferry, R. M. Briggs, H. A. Atwater, *Nat. Commun.* 2011, **2**, 517.

CAS | PubMed | Web of Science® | Google Scholar

12 Y. Cui, J. Xu, K. H. Fung, Y. Jin, A. Kumar, S. He, N. X. Fang, *Appl. Phys. Lett.* 2011, **99**, 253101.

CAS | Web of Science® | Google Scholar

13 L. Huang, D. R. Chowdhury, S. Ramani, M. T. Reiten, S.-N. Luo, A. J. Taylor, H.-T. Chen, *Opt. Lett.* 2012, **37**, 154.

PubMed | Web of Science® | Google Scholar

14 M. G. Nielsen, A. Pors, O. Albrektsen, S. I. Bozhevolnyi, *Opt. Express* 2012, **20**, 13311.

PubMed | Web of Science® | Google Scholar

15 J. Zhu, Z. Ma, W. Sun, F. Ding, Q. He, L. Zhou, Y. Ma, *Appl. Phys. Lett.* 2014, **105**, 021102.

CAS | Web of Science® | Google Scholar

16 T. Søndergaard, S. M. Novikov, T. Holmgaard, R. L. Eriksen, J. Beermann, Z. Han, K. Pedersen, S. I. Bozhevolnyi, *Nat. Commun.* 2012, **3**, 969.

CAS | PubMed | Web of Science® | Google Scholar

17 J. Beermann, R. L. Eriksen, T. Søndergaard, T. Holmgaard, K. Pedersen, S. I. Bozhevolnyi, *New J. Phys.* 2013, **15**, 073007.

CAS | Web of Science® | Google Scholar

18 Y. Cui, K. H. Fung, J. Xu, H. Ma, Y. Jin, S. He, N. X. Fang, *Nano Lett.* 2012, **12**, 1443.

CAS | PubMed | Web of Science® | Google Scholar

19 F. Ding, Y. Cui, X. Ge, Y. Jin, S. He, *Appl. Phys. Lett.* 2012, **100**, 103506.

CAS | Web of Science® | Google Scholar

20 F. Ding, Y. Jin, B. Li, H. Cheng, L. Mo, S. He, *Laser Photonics Rev.* 2014, **8**, 946.

Web of Science® | Google Scholar

21 S. He, F. Ding, L. Mo, F. Bao, *Prog. Electromagn. Res.* 2014, **147**, 69.

Web of Science® | Google Scholar

22 S. AbdollahRamezani, K. Arik, S. Farajollahi, A. Khavasi, Z. Kavehvash, *Opt. Lett.* 2015, **40**, 5383.

PubMed | Web of Science® | Google Scholar

23 J. Gu, R. Singh, X. Liu, X. Zhang, Y. Ma, S. Zhang, S. A. Maier, Z. Tian, A. K. Azad, H.-T. Chen, *Nat. Commun.* 2012, **3**, 1151.

CAS | PubMed | Web of Science® | Google Scholar

24 S. Wang, L. Kang, D. H. Werner, *Sci. Rep.* 2017, **7**, 4326.

PubMed | Web of Science® | Google Scholar

25 U. Guler, A. Boltasseva, V. M. Shalaev, *Science* 2014, **344**, 263.

CAS | PubMed | Web of Science® | Google Scholar

26 W. Wang, Y. Qu, K. Du, S. Bai, J. Tian, M. Pan, H. Ye, M. Qiu, Q. Li, *AIP Appl. Phys. Lett.* 2017, **110**, 101101.

CAS | Web of Science® | Google Scholar

27 Y. Liu, C. Wu, X. Gu, Y. Kong, X. Yu, R. Ge, X. Cai, X. Qiang, J. Wu, X. Yang, *Opt. Lett.* 2020, **45**, 73.

CAS | Web of Science® | Google Scholar

28 Z. Liu, G. Liu, X. Liu, J. Chen, C. Tang, *Opt. Lett.* 2023, **48**, 1586.

CAS | PubMed | Web of Science® | Google Scholar

29 X. Lin, C. W. Hsu, G. P. Wang, *Opt. Express* 2016, **24**, 23136.

PubMed | Web of Science® | Google Scholar

30 Z. Liu, G. Liu, Z. Huang, X. Liu, G. Fu, *Sol. Energy Mater. Sol. Cells* 2018, **179**, 346.

CAS | Web of Science® | Google Scholar

31 G. Calajó, F. Ciccarello, D. Chang, P. Rabl, *Phys. Rev. A* 2016, **93**, 033833.

Web of Science® | Google Scholar

32 C. Ciuti, I. Carusotto, *Phys. Rev. A* 2006, **74**, 033811.

CAS | Web of Science® | Google Scholar

33 S. Zhang, D. A. Genov, Y. Wang, M. Liu, X. Zhang, *Phys. Rev. Lett.* 2008, **101**, 047401.

CAS | PubMed | Web of Science® | Google Scholar

34 T. Rudolph, Z. Ficek, B. Dalton, *Phys. Rev. A* 1995, **52**, 636.

CAS | PubMed | Google Scholar

35 S. Zou, G. C. Schatz, *J. Chem. Phys.* 2004, **121**, 12606.

CAS | PubMed | Web of Science® | Google Scholar

36 X. Su, B. Ham, *Phys. Rev. A* 2005, **71**, 013821.

Google Scholar

37 R. Degl'Innocenti, S. Zanotto, A. Tredicucci, G. Biasiol, L. Sorba, *Solid State Commun.* 2011, **151**, 1725.

Web of Science® | Google Scholar

38 M. D. Lukin, M. Fleischhauer, M. O. Scully, V. L. Velichansky, *Opt Lett* 1988, **23**, 295.

Google Scholar

39 A. Yariv, P. Yeh, in *Optical Waves in Crystals*, Wiley, New York 1984.

Google Scholar

40 H.-F. Zhang, P.-W. Zhai, X.-M. Su, J.-H. Wu, J.-Y. Gao, *Phys. Rev. A* 2002, **65**, 043812.

Google Scholar

41 R. Feng, J. Qiu, L. Liu, W. Ding, L. Chen, *Opt. Express* 2014, **22**, A1713.

PubMed | Web of Science® | Google Scholar